# Microwave Photonic Frequency Measurement With Large Bandwidth Enabled by Multiple Frequency-to-Time Mapping Curves

Boyang Ni<sup>®</sup>, Dan Zhu<sup>®</sup>, Zhouyang Pan<sup>®</sup>, Jiewen Ding<sup>®</sup>, and Shilong Pan<sup>®</sup>, Fellow, IEEE, Fellow, Optica

Abstract—A microwave photonic frequency measurement system with a large bandwidth enabled by multiple frequency-to-time mapping (FTTM) curves is proposed and demonstrated. The optical sideband of the signal under test (SUT) is simultaneously mixed with the multiple frequency-sweeping optical sidebands generated from a semiconductor laser working in the period-one state. Multiple FTTM curves are achieved in a single channel due to the use of multiple frequency-sweeping optical sidebands and the square-law detection feature of the photodetector. The mixing products then pass through an electrical bandpass filter and an envelope detector to obtain electrical pulses at low speed. Multiple FTTM curves are exploited jointly to map the frequency of the SUT to the number and time locations of the generated electrical pulses, which can be captured with a low sampling rate. In this way, without introducing complex structures, the measurement bandwidth of the system can be effectively increased while guaranteeing the time and frequency resolutions. In a proof-of-concept experiment, four FTTM curves are realized by using the  $-1^{st}$ and the  $-2^{nd}$ -order frequency-sweeping optical sidebands. The instantaneous measurement bandwidth is extended to 39.8 GHz, with the working frequency range from 7.6 to 47.4 GHz and a root-mean-square error of 35 MHz. The frequency resolution is better than 50 MHz when the sweeping period is 50  $\mu$ s.

Index Terms—Filter-based frequency-to-time mapping, multiple frequency-to-time mapping curves, photonics-based microwave frequency measurement.

# I. INTRODUCTION

ICROWAVE frequency measurement technology is widely applied in civil and defense applications, such as cognitive radio systems [1], [2], radar [3], electronic warfare systems [4], and wireless communication systems [5]. The photonics-based microwave frequency measurement techniques have been proven to provide distinct features in terms of excellent reconfigurability and tunability, large working bandwidth, and immunity to electromagnetic interference thanks to the

Received 31 May 2025; revised 8 August 2025; accepted 17 August 2025. Date of publication 20 August 2025; date of current version 2 October 2025. This work was supported by the Natural Science Foundation of Jiangsu Province under Grant BK20220076. (Corresponding author: Dan Zhu.)

The authors are with the National Key Laboratory of Microwave Photonics, College of Electronic and Information Engineering, Nanjing University of Aeronautics and Astronautics, Nanjing 210016, China (e-mail: nby\_01@nuaa.edu.cn; danzhu@nuaa.edu.cn; pan\_zy@nuaa.edu.cn; dingjw@nuaa.edu.cn; pans@nuaa.edu.cn).

Color versions of one or more figures in this article are available at https://doi.org/10.1109/JLT.2025.3600877.

Digital Object Identifier 10.1109/JLT.2025.3600877

advantages introduced by photonics [6]. The photonics-based microwave frequency measurement methods are mainly based on frequency-to-power mapping (FTPM), frequency-to-space mapping (FTSM), and frequency-to-time mapping (FTTM).

For the FTPM methods, a frequency-dependent amplitude comparison function (ACF) is constructed, which is defined by the microwave or optical power ratio between two parallel channels. The frequency can be measured from the ACF. The two channels with different power responses can be realized based on dispersive elements [7], a Sagnac interferometer [8], a Fano resonator [9], an asymmetrical Mach-Zehnder interferometer (MZI) [10], or a silicon MZI coupled ring array [11]. The FTPM methods show the advantages of a large frequency measurement range and high accuracy, but suffer from difficulty in multi-tone microwave signal measurement. The FTSM method can achieve multi-tone microwave signal measurements by splitting the signal under test (SUT) into several channels. By combining the measurement results from each channel, the spectral information of the SUT can be recovered. Such schemes can be realized by utilizing an optical frequency comb, an optical comb filter, and an optical de-multiplexer [12]. The main drawback of these schemes is the high cost and complexity caused by parallel detection and processing.

The FTTM methods have shown great advantages for measuring wideband and multi-frequency microwave signals. The frequency of the SUT ( $f_{SUT}$ ) is mapped to the time domain through photonic techniques, which can be commonly obtained in the time domain and recovered. The approaches to accomplish the FTTM process mainly include the dispersion-based FTTM and the filter-based FTTM. In the dispersion-based FTTM, an ultra-short optical pulse passes through a dispersive element, an electro-optic modulator, and two complementary dispersive elements. The spectrum of the SUT is mapped to the time domain [13]. To achieve the high frequency resolution, the optical dispersion value needs to be large, bringing a substantial challenge. The frequency resolution of 70 MHz and the frequency range of 2-32 GHz are realized in [14] by using the  $\pm 2$ nd modulated optical sidebands to achieve the frequency stretch in the optical domain. In [15], the frequency resolution is further improved to 30 MHz by introducing time compression in the optical domain to achieve a frequency magnification factor of 7.

In comparison, the filter-based FTTM schemes provide distinct features in terms of frequency resolution. The fundamental

0733-8724 © 2025 IEEE. All rights reserved, including rights for text and data mining, and training of artificial intelligence and similar technologies. Personal use is permitted, but republication/redistribution requires IEEE permission. See https://www.ieee.org/publications/rights/index.html for more information.

idea is to mix the SUT with a reference signal, and the mixing result is sent into a bandpass filter to generate pulses. By sweeping the frequency of the reference signal or the center frequency of the bandpass filter, the position of the generated pulse is correlated with the frequency of the SUT. Accordingly, to realize the filter-based FTTM, there are two primary approaches. For the first one, the SUT is mixed with a chirped signal by using photonics technology, and the mixing result is selected by a fixed electrical bandpass filter (EBPF) [16], [17], [18], a dispersion-induced photonic filter [19], or an optical bandpass filter (OBPF) [20]. For the second method, a frequency-sweeping filter is applied to detect the RF signal under test modulated onto a fixed optical carrier. The signal pulse will be observed when the center frequency of the sweeping filter is aligned with the  $f_{\rm SUT}$ , from which the frequency of the SUT can be estimated [21].

For the microwave photonic frequency measurement approaches employing filter-based FTTM methods, the instantaneous analysis bandwidth is limited by the sweeping range of the frequency-sweeping signal or the scanning filter. What's more, the increase in the sweeping bandwidth in a single channel will result in the deterioration of the time or frequency resolution. To solve this problem, in [22], the OFC-based channelization scheme is introduced to improve the working bandwidth without reducing the frequency and time resolutions. In [23], by employing photonic in-phase and quadrature (I/Q) frequency mixing to distinguish and measure the RF signals in two frequency bands being imaged to each other, the analysis bandwidth is extended to be twice the actual frequency-sweeping range. The channelized structure or the photonic I/Q mixing structure makes the system complex.

In this article, a microwave photonic frequency measurement scheme based on multiple frequency-to-time mapping curves is proposed and demonstrated. The microwave signal to be measured is mixed with multiple frequency-sweeping signals simultaneously with the help of photonic techniques. In this way, multiple frequency-to-time mapping curves are implemented in a single channel. The frequency of the SUTs is mapped to the number and locations of the output electrical pulses in the time domain. In this way, without introducing complex structures, the analysis bandwidth of the system is effectively increased while guaranteeing the time and frequency resolutions. In a proof-of-concept experiment, four FTTM curves are realized by two chirped optical sidebands generated from an optically injected semiconductor laser. The instantaneous analysis bandwidth is extended to 39.8 GHz, with a measurement range from 7.6 to 47.4 GHz and a root-mean-square error of 35 MHz. The frequency resolution is better than 50 MHz when the sweeping period is 50  $\mu$ s.

#### II. PRINCIPLE

The schematic diagram of the proposed microwave frequency measurement system enabled by multiple frequency-to-time mapping curves is shown in Fig. 1(a). In the system, a continuous optical carrier with a frequency of  $f_c$  is emitted from the master laser (ML) and split into two branches. The optical spectra of the injected optical signal and the free-running slave laser (SL) are shown in Fig. 1(b). In the upper branch, under the injection

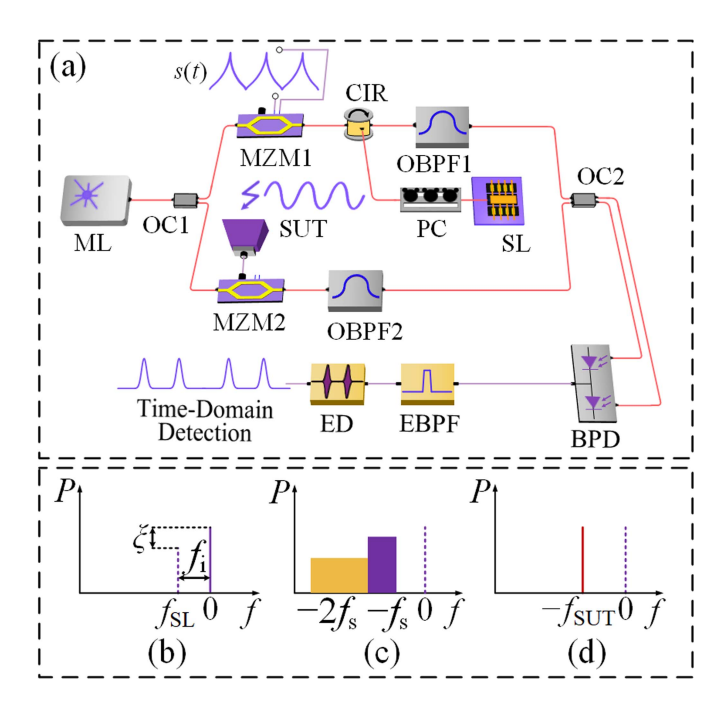


Fig. 1. (a) The schematic configuration of the proposed microwave photonic frequency measurement system with a large bandwidth enabled by multiple frequency-to-time mapping curves. ML: master laser; OC: Optical coupler; MZM: Mach-zehnder modulator; s(t): Quasi-triangular wave control signal; CIR: Circulator; PC: Polarization controller; SL: Slave laser; OBPF: Optical bandpass filter; SUT: Signal under test; BPD: Balanced photodetector; EBPF: Electrical bandpass filter; ED: Envelope detector. (b) The optical spectra of the injected optical signal and the free-running SL. (c) and (d) The optical spectra at the output of OBPF1 and OBPF2.

of an intensity-modulated signal, the period-one (P1) dynamics of the SL can be excited, and a series of periodic bidirectional frequency-sweeping optical sidebands are generated. An OBPF (OBPF1) selectively filters two of the chirped optical sidebands, as depicted in Fig. 1(c). In the lower branch, by applying an MZM and an OBPF (OBPF2), the -1st-order modulated optical sideband of a SUT is generated, as illustrated in Fig. 1(d). The optical signals output from the two branches are coupled and then divided into two parts and injected into a balanced photodetector (BPD). In this way, the optical sideband of a SUT is simultaneously mixed with the two frequency-sweeping optical sidebands. Each mixing product is an electrical frequencysweeping signal, whose central frequency is determined by the frequency of the SUT. The signal output from the BPD then passes through an EBPF, and the electrical pulses will be generated, for which the frequency of the SUT determines the number and time positions. By detecting the envelopes of the output electrical pulses, the number and the time positions of the pulses can be identified, from which the frequency of the SUT will be obtained.

In the upper branch, the optical carrier is modulated by a quasitriangular wave control signal s(t) at MZM1. The intensity-modulated optical carrier is injected into the semiconductor SL with a frequency of  $f_{\rm SL}$  through an optical circulator (CIR) and a polarization controller (PC). By regulating the injection strength  $\xi$  and the detuning frequency  $f_{\rm i}$  shown in Fig. 1(b), the P1 state of the SL can be excited. The optical spectrum of the SL in the P1 state is characterized as the asymmetric double sideband

modulation with a modulation frequency of the P1 frequency  $f_{\rm s}$  and the optical carrier frequency of  $f_{\rm c}$ . Herein,  $f_{\rm c}$  is normalized to 0 for simplicity. The P1 frequency  $f_{\rm s}$  will increase with the increase of  $\xi$  for a fixed detuning frequency  $f_{\rm i}$ . Therefore, a series of periodic bidirectional chirped optical sidebands are generated from the SL injected by the intensity-modulated optical carrier [24], [25]. The signal output from the SL is then routed into OBPF1 through the CIR, and only the -1st and -2nd-order frequency-sweeping optical sidebands remain, as illustrated in Fig. 1(c). Taking one sweeping period as an example, the electrical field of the optical signal output from OBPF1 can be written as

$$E_{\rm U}(t) = E_1 \exp\left[-j2\pi f_{\rm s}(t) t\right] + E_2 \exp\left[-j4\pi f_{\rm s}(t) t\right], t \in (0, T],$$
 (1)

where  $E_1$  and  $E_2$  denote the amplitudes of the  $-1^{st}$  and  $-2^{nd}$ order frequency-sweeping optical sidebands, respectively; Tstand for the sweeping period.

In the lower branch, the SUT is modulated to the optical carrier at MZM2. The -1st-order modulated optical sideband is selected by OBPF2, with the expression as follows

$$E_{\rm L}(t) = E_{\rm SUT} \exp\left(-j2\pi f_{\rm SUT}t\right),\tag{2}$$

where  $E_{SUT}$  indicates the amplitude of  $E_{L}(t)$ , while  $f_{SUT}$  refers to the frequency of the SUT.

The optical outputs from the upper and the lower branches are combined and then divided into two parts by using a  $2\times2$  optical coupler (OC, OC2), which follows the expression as follows:

$$\begin{cases}
E_{\mathrm{C},1}(t) \propto E_{\mathrm{U}}(t) + \mathrm{j}E_{\mathrm{L}}(t) \\
E_{\mathrm{C},2}(t) \propto \mathrm{j}E_{\mathrm{U}}(t) + E_{\mathrm{L}}(t).
\end{cases}$$
(3)

These optical signals are then input into the BPD, with the electrical output given as follows,

$$\begin{cases} I_{\text{BPD}}(t) \propto |E_{\text{C},1}(t)|^2 - |E_{\text{C},2}(t)|^2 \\ \propto |E_{\text{U}}(t) + jE_{\text{L}}(t)|^2 - |jE_{\text{U}}(t) + E_{\text{L}}(t)|^2 \\ = 4E_{\text{U}}(t) E_{\text{L}}^*(t) \\ = 4E_{\text{SUT}}E_1 \exp\left(j2\pi f_{\text{BPD},1}t\right) \\ + 4E_{\text{SUT}}E_2 \exp\left(j2\pi f_{\text{BPD},2}t\right), t \in (0,T] \\ f_{\text{BPD},1} = |f_{\text{SUT}} - f_{\text{s}}(t)| \\ f_{\text{BPD},2} = |f_{\text{SUT}} - 2f_{\text{s}}(t)|. \end{cases}$$
(4)

It can be seen that the output electrical signal contains the mixing results of  $f_{\rm SUT}$  with two sweeping frequencies,  $f_{\rm s}$  and  $2f_{\rm s}$ , respectively. The two mixing results are defined as  $f_{\rm BPD,1}$  and  $f_{\rm BPD,2}$ , respectively, whose frequencies sweep over time. Then, the output electrical signal passes through an EBPF. Since only the components within a specific narrow frequency band are selected by the EBPF, pulse signals will be generated. An electrical pulse will be generated when  $f_{\rm BPD,1}$  or  $f_{\rm BPD,2}$  is identical to the center frequency  $f_{\rm F}$  of the EBPF. The envelopes of the electrical pulses in the time domain can be obtained by using an envelope detector (ED). The time position of the pulse signal is determined by the frequency to be measured. According to (4), the four conditions for pulse generation can be expressed as  $f_{\rm SUT}-f_{\rm S}=f_{\rm F},f_{\rm S-}f_{\rm SUT}=f_{\rm F},f_{\rm SUT}=2f_{\rm F}$ , and  $2f_{\rm S-}f_{\rm SUT}=f_{\rm S-}f_{\rm SUT}=f_{\rm F}$ ,  $f_{\rm SUT}=f_{\rm F},f_{\rm SUT}=f_{\rm F}$ , and  $2f_{\rm S-}f_{\rm SUT}=f_{\rm SUT}=f_{\rm S-}f_{\rm S-}f_{\rm SUT}=f_{\rm S-}f_{\rm S-}f$ 

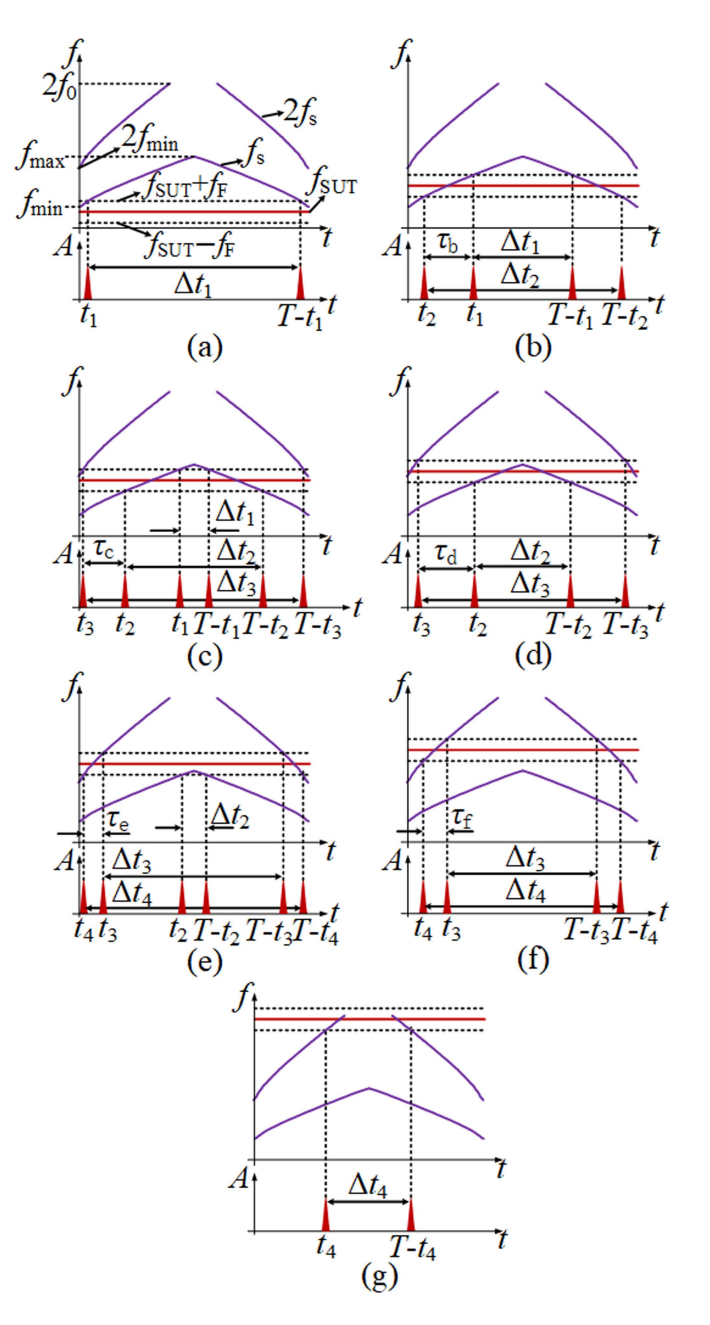


Fig. 2. The illustration of the generated pulses distribution, when  $f_{\rm SUT}$  is within (a)  $[f_{\rm min}-f_{\rm F},f_{\rm min}+f_{\rm F})$ , (b)  $[f_{\rm min}+f_{\rm F},2f_{\rm min}-f_{\rm F})$ , (c)  $[2f_{\rm min}-f_{\rm F},f_{\rm max}-f_{\rm F})$ , (d)  $[f_{\rm max}-f_{\rm F},2f_{\rm min}+f_{\rm F})$ , (e)  $[2f_{\rm min}+f_{\rm F},f_{\rm max}+f_{\rm F})$ , (f)  $[f_{\rm max}+f_{\rm F},2f_0-f_{\rm F})$  and (g)  $[2f_0-f_{\rm F},2f_0+f_{\rm F})$ .

 $f_{\rm F}$ . Each equation represents an FTTM curve. Due to the use of bidirectional frequency sweeping, as shown in Fig. 2, a pair of pulses symmetric about the center of the sweeping period will be generated when  $f_{\rm s}$  or  $2f_{\rm s}$  is identical to  $f_{\rm SUT}-f_{\rm F}$  or  $f_{\rm SUT}+f_{\rm F}$ . The time intervals between a pair of pulses are denoted as  $\Delta t_1$ ,  $\Delta t_2$ ,  $\Delta t_3$ , and  $\Delta t_4$  for the conditions of  $f_{\rm s}=f_{\rm SUT}+f_{\rm F}$ ,  $f_{\rm s}=f_{\rm SUT}-f_{\rm F}$ ,  $2f_{\rm s}=f_{\rm SUT}+f_{\rm F}$ , and  $2f_{\rm s}=f_{\rm SUT}-f_{\rm F}$ , respectively.

The relationship curves between  $f_{\rm SUT}$  and  $\Delta t_1$ ,  $\Delta t_2$ ,  $\Delta t_3$ , and  $\Delta t_4$  are denoted as FTTM1, FTTM2, FTTM3, and FTTM4, as shown in Fig. 3. The frequency measurement ranges of the four FTTM curves partially overlap. By using the four FTTM curves, the measurement bandwidth will be effectively extended. The frequency of the input microwave signal is mapped to the number

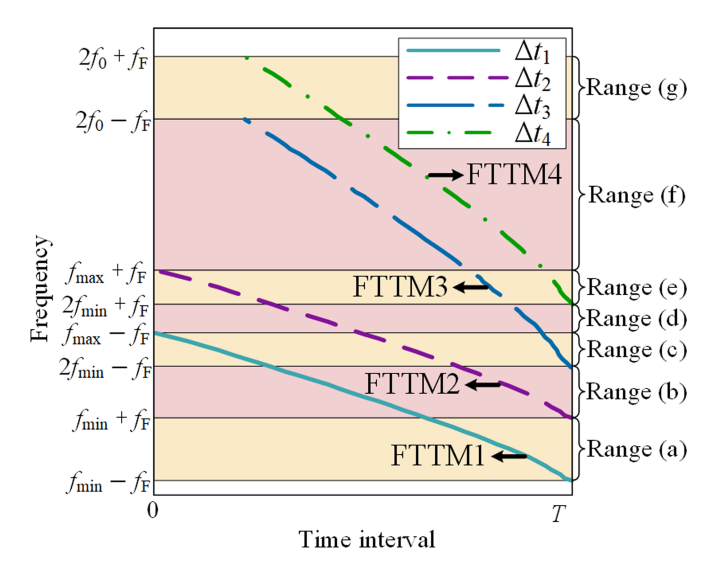


Fig. 3. The multiple frequency-to-time mapping curves illustration for the proposed system. FTTM1  $\sim$  FTTM4 are generated from  $f_{\rm SUT} = f_{\rm s} - f_{\rm F}, f_{\rm SUT} = f_{\rm s} + f_{\rm F}, f_{\rm SUT} = 2f_{\rm s} - f_{\rm F}, \text{ and } f_{\rm SUT} = 2f_{\rm s} + f_{\rm F}, \text{ respectively.}$ 

and locations of the output electrical pulses. A single-frequency microwave signal may result in more than one pair of electrical pulses due to the use of four FTTM curves. By jointly analyzing the output electrical pulses, the frequency of the SUT can be obtained over a large bandwidth.

For the SUTs with different frequencies, the distribution of generated electrical pulses will undergo 7 categories as shown in Fig. 2(a)–(g), respectively. As can be seen, the electrical pulses will be generated when  $f_{\rm s}$  or  $2f_{\rm s}$  is identical to  $f_{\rm SUT}-f_{\rm F}$  or  $f_{\rm SUT}+f_{\rm F}$ . As shown in Fig. 2(a), the ranges of  $f_{\rm s}$  and  $2f_{\rm s}$  are given as  $f_{\rm min} \sim f_{\rm max}$  and  $2f_{\rm min} \sim 2f_{\rm 0}$ , respectively.  $2f_{\rm 0}$  is defined as the maximum value of  $2f_{\rm s}$ . As  $f_{\rm s}$  increases, the amplitudes of the frequency-sweeping optical sidebands decrease. For this reason,  $f_{\rm 0}$  is usually less than  $f_{\rm max}$ .

For range (a),  $f_{SUT}$  satisfies  $f_{min} - f_{F} \le f_{SUT} < f_{min} + f_{F}$ . For this condition, a pair of pulses is generated, and  $f_{\rm SUT}$  is mapped to  $\Delta t_1$ , which is obtained by taking  $\Delta t_1$  into FTTM1. For range (b),  $f_{SUT}$  satisfies  $f_{min} + f_F \le f_{SUT} < 2f_{min} - f_F$ . Here, two pairs of pulses will be generated, and  $f_{SUT}$  is mapped to  $\Delta t_1$  and  $\Delta t_2$  simultaneously. Thus,  $f_{\rm SUT}$  can be obtained by taking  $\Delta t_1$  and  $\Delta t_2$  into FTTM1 and FTTM2, respectively. For range (c),  $f_{SUT}$  satisfies  $2f_{min} - f_F \le f_{SUT} < f_{max} - f_F$ . Three pairs of pulses will be generated, and  $f_{SUT}$  is mapped to  $\Delta t_1$ ,  $\Delta t_2$ , and  $\Delta t_3$  simultaneously. For this condition,  $f_{\rm SUT}$  can be calculated by taking  $\Delta t_1$ ,  $\Delta t_2$ , and  $\Delta t_3$  into FTTM1, FTTM2, and FTTM3, respectively. For range (d),  $f_{SUT}$  satisfies  $f_{max}$  –  $f_{\rm F} \le f_{\rm SUT} < 2f_{\rm min} + f_{\rm F}$ . Here, two pairs of pulses are generated.  $f_{\rm SUT}$  is mapped to  $\Delta t_2$  and  $\Delta t_3$ , simultaneously, which can be calculated by taking  $\Delta t_2$  and  $\Delta t_3$  into FTTM2 and FTTM3, respectively. For range (e), we have  $2f_{\min} + f_{\text{F}} \leq f_{\text{SUT}} < f_{\max}$  $+f_{\rm F}$ . Three pairs of pulses will be generated, and  $f_{\rm SUT}$  is mapped to  $\Delta t_2$ ,  $\Delta t_3$ , and  $\Delta t_4$  simultaneously.  $f_{\rm SUT}$  can be calculated by taking  $\Delta t_2$ ,  $\Delta t_3$ , and  $\Delta t_4$  into FTTM2, FTTM3, and FTTM4, respectively. For range (f),  $f_{\text{max}} + f_{\text{F}} \le f_{\text{SUT}} < 2f_0 - f_{\text{F}}$ . Two pairs of pulses will be generated, and  $f_{SUT}$  is mapped to  $\Delta t_3$ 

and  $\Delta t_4$  simultaneously.  $f_{\rm SUT}$  can be measured by taking  $\Delta t_3$  and  $\Delta t_4$  into FTTM3 and FTTM4, respectively. For range (g),  $2f_0 - f_{\rm F} \leq f_{\rm SUT} < 2f_0 + f_{\rm F}$ . Only one pair of pulses with a time interval of  $\Delta t_4$  will be generated. Thus,  $f_{\rm SUT}$  can be calculated by taking  $\Delta t_4$  into FTTM4.

The pulse distributions that have the same pulse number need to have other characteristics so that they can be distinguished. It can be roughly considered that  $f_{\rm s}$  sweeps linearly for ease of analysis. For ranges (a) and (g) shown in Fig. 3, only one pair of pulses will be generated for each period. The two ranges can be distinguished by the time interval between the two pulses in a sweeping period. The time intervals in Fig. 2(a) and (g) are separately defined as  $\Delta t_1$  and  $\Delta t_4$ . For the condition shown in Fig. 2(a), when  $f_{\rm SUT} = f_{\rm min} + f_{\rm F}$ ,  $\Delta t_1$  reaches the minimum value  $(T-4f_{\rm F}/k_{\rm s})$ , where  $k_{\rm s}$  is the sweeping rate of  $f_{\rm s}$ . For the condition shown in Fig. 2(g), when  $f_{\rm SUT} = 2f_0 - f_{\rm F}$ ,  $\Delta t_4$  reaches the maximum value of  $[T-2(f_0-f_{\rm F}-f_{\rm min})/k_{\rm s}]$ . Thus, the generated pulses for range (a) and range (g) in Fig. 3 can be distinguished by setting  $f_{\rm min} + 3f_{\rm F} < f_0$  to make  $(T-4f_{\rm F}/k_{\rm s}) > [T-2(f_0-f_{\rm F}-f_{\rm min})/k_{\rm s}]$ .

For ranges (b), (d), and (f) in Fig. 3, the generated number of pulse pairs is 2. These three ranges can be distinguished by the time interval ( $\tau_{\rm b}$ ,  $\tau_{\rm d}$ , and  $\tau_{\rm f}$  defined in Fig. 2(b), (d), and (f)) of the two pulses in the first half sweeping period. In range (b), as  $f_{\rm SUT}$  changes,  $\tau_{\rm b}$  remains a constant of  $2f_{\rm F}/k_{\rm s}$ , as shown in Fig. 2(b). In range (f),  $\tau_{\rm f}$  also remains a constant of  $f_{\rm F}/k_{\rm s}$  as shown in Fig. 2(f). As can be seen,  $\tau_{\rm b}$  is always greater than  $\tau_{\rm f}$ . In range (d),  $\tau_{\rm d}$  will reach the minimum value of  $(f_{\rm max}/2-2f_{\rm F})/k_{\rm s}$  when  $f_{\rm SUT}=f_{\rm max}-f_{\rm F}$ . By setting  $f_{\rm max}>8f_{\rm F}$ , the relationship of  $(f_{\rm max}/2-2f_{\rm F})/k_{\rm s}>2f_{\rm F}/k_{\rm s}$  can be satisfied. In this way,  $\tau_{\rm b}$ ,  $\tau_{\rm d}$ , and  $\tau_{\rm f}$  always have the relationship of  $\tau_{\rm d}>\tau_{\rm b}=2f_{\rm F}/k_{\rm s}=2\tau_{\rm f}$ , so ranges (b), (d), and (f) can be distinguished.

For ranges (c) and (e) in Fig. 3, the system outputs three pairs of pulses. The two ranges can be identified by the time intervals ( $\tau_{\rm c}$  and  $\tau_{\rm e}$  defined in Fig. 2(c) and (e)) of the first two pulses. In range (e),  $\tau_{\rm e}$  has a constant value of  $f_{\rm F}/k_{\rm s}$  and does not vary with  $f_{\rm SUT}$ . In range (c), the minimum value of  $\tau_{\rm c}$  can be achieved as  $(f_{\rm min}-2f_{\rm F})/k_{\rm s}$  when  $f_{\rm SUT}=2f_{\rm min}-f_{\rm F}$ .  $\tau_{\rm c}$  can always be larger than  $\tau_{\rm e}$  by setting  $f_{\rm min}>3f_{\rm F}$  to make  $(f_{\rm min}-2f_{\rm F})/k_{\rm s}$  larger than  $f_{\rm F}/k_{\rm s}$ . In this way, ranges (c) and (e) can be distinguished.

In conclusion, the measurement ambiguity can be avoided for all the conditions in Figs. 2 and 3, when the following relationships are satisfied,

$$\begin{cases} f_{\min} + 3f_{\mathrm{F}} < f_{0} \\ f_{\max} > 8f_{\mathrm{F}} \\ f_{\min} > 3f_{\mathrm{F}} \end{cases}$$
 (5)

The joint utilization of four FTTM curves is the main highlight of this work for the enhancement of the performance of the microwave frequency measurement achieved by filter-based FTTM. By joint utilization of four FTTM curves, the measurement range of  $f_{\rm min}-f_{\rm F}\sim 2f_0+f_{\rm F}$  can be achieved. and the measurement bandwidth is  $2f_0-f_{\rm min}+2f_{\rm F}$ . In comparison, the measurement bandwidth is  $B_{\rm s}=f_{\rm max}-f_{\rm min}$  when only one

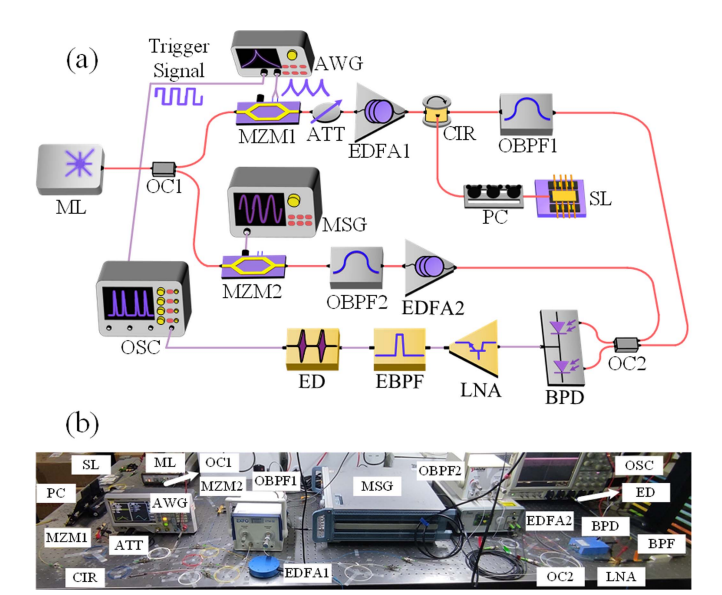


Fig. 4. (a) The experimental setup and (b) the photograph of the proposed microwave photonic frequency measurement system with a large bandwidth enabled by multiple frequency-to-time mapping curves. AWG: arbitrary waveform generator; ATT: attenuator; EDFA: Erbium-doped fiber amplifier; MSG: Microwave signal generator; LNA: Low noise amplifier; OSC: Oscilloscope.

FTTM curve is used. Since  $2f_0$  can be larger than  $f_{\text{max}}$ , the measurement bandwidth is extended.

#### III. EXPERIMENTAL RESULTS AND DISCUSSIONS

# A. Experimental Setup

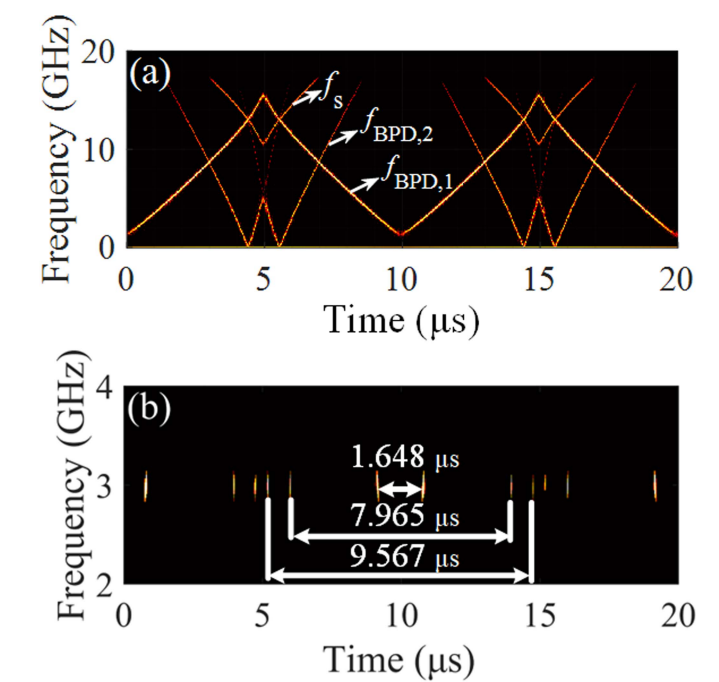
Based on the system diagram illustrated in Fig. 1(a), a proofof-concept experiment is conducted with the setup shown in Fig. 4. The ML (Keysight, N7714A) generates a continuous lightwave with a frequency of 193.5825 THz and a power of 16 dBm. The electrical control signal is generated from an arbitrary waveform generator (AWG, RIGOL, DG4102) with a sampling rate of 500 MSa/s. MZM1 (iXblue, MXER-LN-10) has a 3-dB bandwidth of 10 GHz and a half-wave voltage of 5.5 V at 50 kHz. A photonic attenuator with an attenuation range of 30 dB, followed by EDFA1, is utilized to achieve a wide power variation range with the injected optical signal. EDFA1 (Amonics, AEDFA-16-miniC-FA) operates in the automatic current control mode. The SL is a distributed feedback laser diode (PD-LD, PL-DFB-1550-C) with a line width of 2 MHz. OBPF1 and OBPF2 (Yenista, XTM-50) have an out-of-band suppression ratio larger than 40 dB. MZM2 (EOSPACE, AX-0MVS-65) has a 6-dB bandwidth of 65 GHz and a half-wave voltage of 5.0 V at 1 GHz. The RF signals to be measured are generated by microwave signal generators (MSG, ROHDE&SCHWARZ, SMA100B). EDFA2 (Amonics, AEDFA-PA-35-B-FA) has an optical gain of 30 dB at -10 dBm and an operation wavelength of 1530 to 1563 nm. The BPD has a 3-dB bandwidth of 17 GHz and a responsivity of 0.94 A/W. The low noise amplifier (LNA, AT Microwave, AT-LNA-0003-5701X) has a working frequency range of 0.1 to 3.5 GHz. The EBPF has a center frequency of 3 GHz and a 6-dB bandwidth of 31 MHz. The ED (Herotek, DZR400KA) has a working frequency range of 10 MHz~40

GHz. The waveforms of the electrical signals are observed by an oscilloscope (Tektronix, DSA72004B) with a tunable sampling rate of up to 50 GSa/s.

Firstly, the generation of the -1st-order and -2nd-order frequency-sweeping optical sidebands is investigated. The electrical control signal is a quasi-triangular wave signal with a voltage from -3.4 to 1.8 V and a 10- $\mu$ s period. The purpose of using a quasi-triangular wave signal is to compensate for the nonlinearity of the time-frequency relationship of the frequency sweeping optical sidebands. As shown in Fig. 4, a square wave signal synchronized with the control signal output by the AWG is used as the trigger signal for the oscilloscope. By this means, the center position of each collected data corresponds to the midpoint of a sweeping period. Therefore, the data within a single measurement cycle can be accurately identified. The SL has an output power of 12.6 dBm and a frequency of 193.5773 THz when operating freely. The average optical power injected into the SL is 13.95 dBm. With the detuning frequency of 5.2 GHz, the SL is controlled at the P1 oscillation state. A 26-GHz microwave signal with a power of 10 dBm is injected into the RF port of MZM2. The time-frequency diagram of the electrical signal output from BPD is shown in Fig. 5(a). As can be seen, the needed bidirectional frequency-sweeping signals (defined as  $f_{\rm BPD,1}$  and  $f_{\rm BPD,2}$  in (4)) to realize the multiple FTTM curves are generated. Meanwhile, the undesired mixing results between the -1st-order frequency-sweeping optical sideband and the optical carrier also exist. The experimentally obtained time-frequency diagram of the signal output from the EBPF is shown in Fig. 5(b). As can be seen, after passing through the EBPF, only the components within the narrow band around 3 GHz are retained, thus pulse signals with time intervals of 1.648, 7.965, and 9.567  $\mu$ s are generated. The generated pulses satisfy the pulse distribution condition shown in Fig. 2(e), and also the distribution feature of range (e) shown in Fig. 3. The P1 frequency  $f_s$  can be given by 26 GHz  $-f_{\rm BPD,1}$ , with the results shown in Fig. 5(c). The P1 frequency varies approximately linearly from 10.6 to 24.7 GHz within a period of 10  $\mu$ s.

# B. Microwave Frequency Measurement With Enhanced Bandwidth

The working bandwidth and the accuracy of the system are then experimentally investigated. The actual FTTM relationships are experimentally calibrated. The SUT is set to be a single-frequency signal. According to the theoretical analyses in Fig. 2 and Fig. 3, the minimum measurable frequency of the system is  $f_{\rm min}-f_{\rm F}=7.6$  GHz. Thus, the SUT's frequency is firstly set to be 7.6 GHz. Then the SUT's frequency is adjusted from 7.8 to 47.4 GHz with a 0.4-GHz step. The experimentally obtained FTTM curves are shown in Fig. 6. The scatters represent the actual measurement results. Fig. 7 reveals the typical obtained temporal waveforms of the electrical pulses in one period output from the system when the frequencies of SUT are set to be 7.6, 16, 20, 22, 26, 33, and 45 GHz, respectively. The waveforms are observed with a sampling rate of 2.5 GSa/s. As can be seen, with the increasing of  $f_{\rm SUT}$ , the mapping results from  $f_{\rm SUT}$  to the



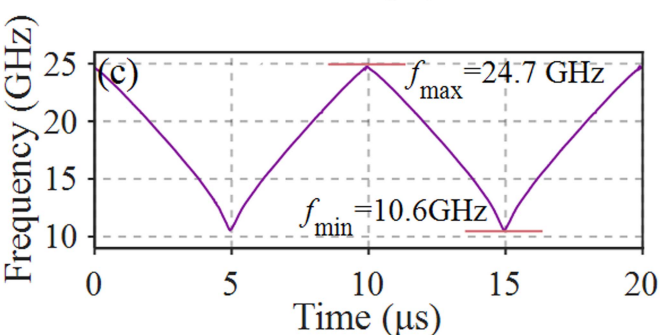


Fig. 5. (a) The experimental result of the time-frequency diagram of the output electrical signal v(t) of BPD when a 26-GHz microwave signal is applied to MZM2; (b) The experimental result of the time-frequency diagram of the output signal from the EBPF; (c) The P1 frequency  $f_s$  versus time, where  $f_s = f_{\rm SUT} - f_{\rm BPD, 1}$ .

number and positions of electrical pulses shown in Fig. 7(a)–(g) agree well with the theoretical analyzing results in Fig. 2(a)–(g).

With the increase of  $f_{\rm SUT}$  from 7.6 to 13.4 GHz, only one pair of electrical pulses is generated, with the measured results forming the part of FTTM1 corresponding to range (a). For Fig. 7(a), when  $f_{\rm SUT}$  is 7.6 GHz, there is only one pair of pulses generated, with a time interval of 10.0044  $\mu$ s. The relationship between the pulse time interval and  $f_{\rm SUT}$  is given as point A in Fig. 6.

Then, with the increasing of  $f_{\rm SUT}$  from 13.8 to 17.8 GHz, two pairs of electrical pulses are generated, with the measured results of the relatively small intervals forming the part of FTTM1 corresponding to range (b), and those of the relatively large intervals forming the part of FTTM2 corresponding to range (b). Typically, for Fig. 7(b), when  $f_{\rm SUT}$  is 16 GHz, two pairs of pulses with time intervals of 4.7528 and 8.8388  $\mu$ s are generated. The relationships between the pulse intervals and  $f_{\rm SUT}$  are marked as points B1 and B2 in Fig. 6.

When  $f_{\rm SUT}$  is within the range of 18.2 to 21.4 GHz, three pairs of electrical pulses are generated. The measured results of the minimum pulse time intervals form the part of FTTM1 in range (c), those of the middle pulse time intervals form the part of FTTM2 in range (c), and those of the maximum pulse time intervals form the part of FTTM3 in range (c). The typical obtained output electrical pulses are shown in Fig. 7(c) with  $f_{\rm SUT}$  of 20 GHz, generating 3 pairs of pulses with time intervals of 1.6512, 6.2556, and 9.5664  $\mu$ s, respectively, described as points C1, C2, and C3 in Fig. 6.

When  $f_{\rm SUT}$  is within the range of 21.8 to 23.8 GHz, two pairs of electrical pulses are generated. The measured results of the minimum pulse time intervals form the part of FTTM2 in range (d), and those of the maximum pulse time intervals form the part of FTTM3 in range (d). Fig. 7(d) shows the output electrical pulses when  $f_{\rm SUT}$  is 22 GHz. Two pairs of pulses with time intervals of 4.7708 and 9.1304  $\mu s$  are generated, shown as points D1 and D2 in Fig. 6.

Then, for the varying range from 24.2 to 27.4 GHz with  $f_{\rm SUT}$ , three pairs of electrical pulses are observed. The measured results of the minimum pulse time intervals form the part of FTTM2 in range (e), those of the middle pulse time intervals form the part of FTTM3 in range (e), and those of the maximum pulse time intervals form the part of FTTM4 in range (e). Fig. 7(e) shows the typical results with  $f_{\rm SUT}$  of 26 GHz. The time intervals for the pairs of pulses are 1.654, 7.9692, and 9.574  $\mu$ s, respectively, shown as points E1, E2, and E3 in Fig. 6.

As  $f_{\rm SUT}$  increases from 27.8 to 41.4 GHz, two pairs of electrical pulses are obtained. The measured results of the minimum pulse time intervals form the part of FTTM3 in range (f), and those of the maximum pulse time intervals form the part of FTTM4 in range (f). Typical output results for  $f_{\rm SUT}$  of 33 GHz are shown in Fig. 7(f), showing 2 pairs of pulses with time intervals of 5.5464 and 7.6648  $\mu$ s, respectively, corresponding to the points F1 and F2 in Fig. 6.

For the frequency range of 41.8 to 47.4 GHz for  $f_{\rm SUT}$ , one pair of electrical pulses will be obtained, with the measured results forming the part of FTTM4 in range (g). For the measured point G in Fig. 6, the  $f_{\rm SUT}$  injected into the system is 45 GHz, and one pair of pulses with a time interval of 3.2696  $\mu s$  is generated, as shown in Fig. 7(g).

The curves in Fig. 6 are the polynomial fitting results for the actual measurement results. It should be noticed that the curves of FTTM3 and FTTM4 introduced by the -2nd-order optical sideband lack the segments for which the time interval of the pulses is less than about 2.303  $\mu$ s. This is because the power of the -2nd-order optical sideband decreases with the increase of the P1 frequency. The maximum measurable frequencies of FTTM3 and FTTM4 are 41.4 and 47.4 GHz, respectively. The frequency of 41.4 GHz is mapped to two pulse intervals of 2.303 and 4.622  $\mu$ s, shown as the points F3 and F4 in Fig. 6. The pulse interval of 2.31  $\mu$ s corresponds to 47.4 GHz, shown as point G1 in Fig. 6. Since the maximum value of  $f_{SUT}$  in FTTM4 is identical to  $2f_0+f_F$ .  $f_0$  can be inferred as 22.2 GHz. The sweeping parameters  $f_{\min}, f_{\max}, f_0$ , and the filter center frequency  $f_{\rm F}$  satisfy the conditions in (5). Therefore, the measurement ambiguity can be avoided for all the 7 conditions, and the system can achieve

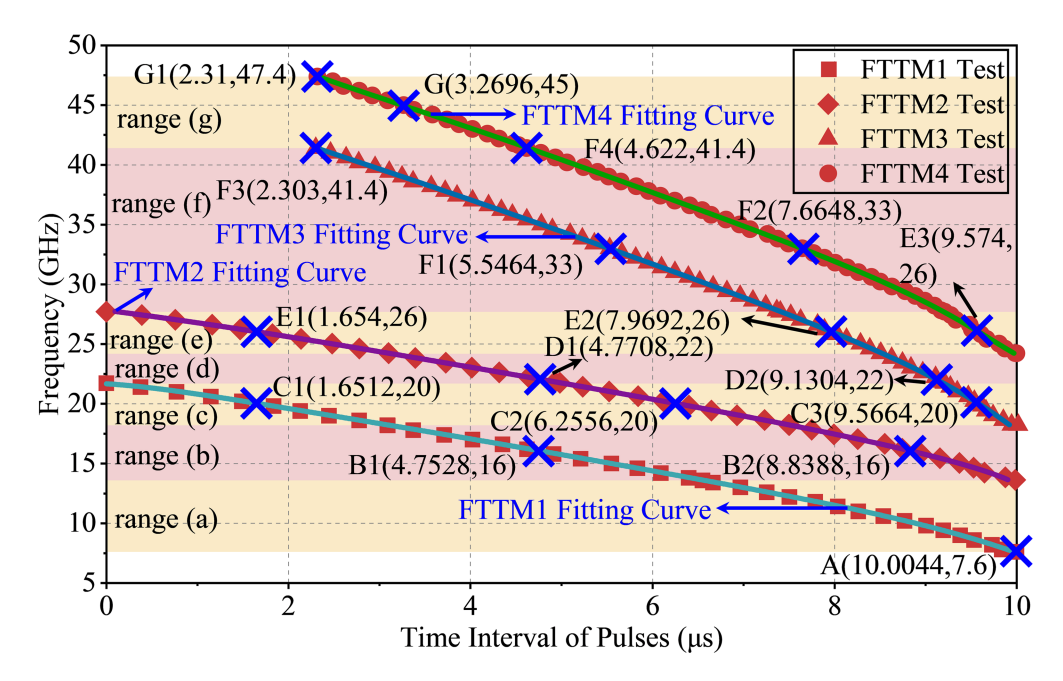


Fig. 6. The experimentally calibrated FTTM curves by fitting the test data.

a frequency measurement range of  $7.6\sim47.4$  GHz. Sub-ranges (a) $\sim$ (g) are marked by different colors in Fig. 6, with the values of  $7.6\sim13.6$  GHz,  $13.6\sim18.2$  GHz, 18.2-21.7 GHz, 21.7-24.2 GHz, 24.2-27.7 GHz, 27.7-41.4 GHz, and 41.4-47.4 GHz, respectively.

Then, using the experimentally obtained curves shown in Fig. 6, the frequencies of the received RF signals can be calculated based on the observed output electrical pulses. As can be seen, by jointly leveraging the four FTTM curves, an instantaneous analysis frequency range of 7.6-47.4 GHz can be achieved.

For the minimum  $f_{SUT}$  of the ranges (a), (b), (c), and (e) shown in Fig. 6, the pulses with a time interval identical to the sweeping period will be generated. For the maximum  $f_{SUT}$  of the ranges (c) and (e) shown in Fig. 6, at the midpoint of each sweeping period, two pulses overlap with each other. The experimental results are shown in Fig. 8. In Fig. 8(a), the pulse waveform is given for the input  $f_{SUT}$  of 13.6 GHz, which is the boundary frequency between ranges (a) and (b) in Fig. 6. Two pairs of pulses with time intervals of 9.994 and 6.548  $\mu$ s are generated, respectively. Here, 9.994  $\mu$ s corresponds to the sweeping period. According to Fig. 6, the measured frequency is 13.592 GHz. Fig. 8(b) illustrates the pulse waveform for  $f_{SUT}$  of 27.7 GHz, which is the boundary  $f_{SUT}$  between ranges (e) and (f) shown in Fig. 6. At the midpoint of the sweeping period, two pulses overlapping with each other exist. According to the experimentally obtained curves of FTTM2, 3, and 4 shown in Fig. 6, the measured frequency is 27.677 GHz. In addition, the frequencies of 18.2, 21.7, 24.2, and 41.6 GHz are also experimentally measured, with the results added in Fig. 6.

The frequency measurement accuracy of the system is also investigated. For each frequency, four measurements are conducted. The measured distributions of electrical pulses are inversely mapped to the measured frequencies by employing the actual FTTM curves shown in Fig. 6. Fig. 9(a) illustrates the

experimentally measured frequency results and error versus the input signal frequencies. A curve fitting is conducted for the scatters, with the result of y = 0.9999x+0.00052. The R-square value is as high as 0.99999. The experimentally obtained measurement error histogram is shown in Fig. 9(b). The maximum error and the root-mean-square error are 108 MHz and 35 MHz, respectively. The error is mainly induced by the frequency instability of the frequency-sweeping optical signal achieved by the P1 oscillations in semiconductor lasers. The measurement accuracy can be upgraded by employing accurate temperature and driving current control [25], [26] or introducing optical-electrical feedback [27], [28].

## C. Multiple Frequencies Measurement

The multiple frequencies measurement capability is also experimentally investigated. Fig. 10(a) shows the output electrical pulse waveforms when two-tone RF signals with frequencies of 10 and 20 GHz are injected. As can be seen, for each period, electrical pulses are generated with time intervals of 9.57, 8.8828, 6.238, and 1.6256  $\mu$ s. Based on Fig. 6, it can be analyzed that 9.57, 6.238, and 1.6256  $\mu$ s are the horizontal coordinates of the intersections of a horizontal line  $f = f_{SUT}$ with FTTM3, FTTM2, and FTTM1. Therefore, the frequencies of the SUT can be obtained by taking 9.57, 6.238, and 1.6256  $\mu$ s into FTTM3, FTTM2, and FTTM1, respectively, with the mapping results 20.071, 20.017, and 20.047 GHz. By averaging the three frequency values, the measured frequency can be obtained as 20.045 GHz. Similarly, the measured frequency of 10.002 GHz can also be obtained by taking 8.8828  $\mu$ s into FTTM1 in Fig. 6. Thus, the measured frequencies of 10.002 and 20.045 GHz are experimentally achieved, agreeing well with the actual frequencies of the input signals.

The multi-tone measurement ability of the system is further verified. The actual input frequency of 10 GHz is unchanged, and the other input RF frequency is changed to 15, 26, and 28 GHz,

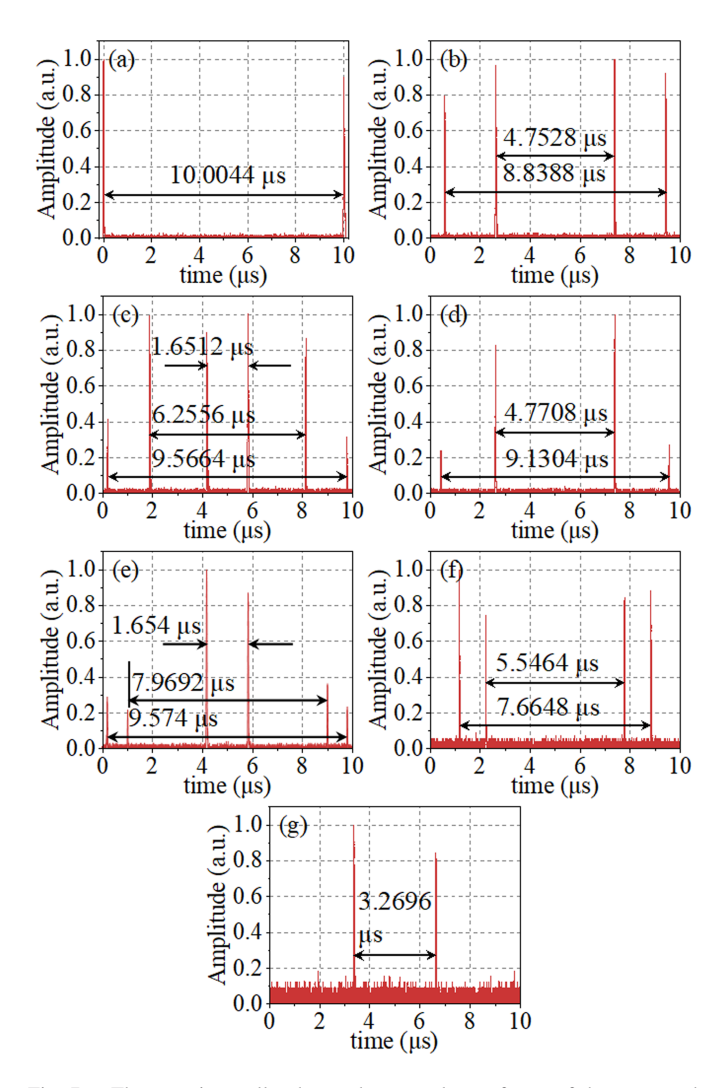


Fig. 7. The experimentally observed temporal waveforms of the generated electrical pulses in each period for (a) 7.6 GHz, (b) 16 GHz, (c) 20 GHz, (d) 22 GHz, (e) 26 GHz, (f) 33 GHz, (g) 45 GHz. (a)–(g) are separately corresponding to Fig. 2(a)–(g).

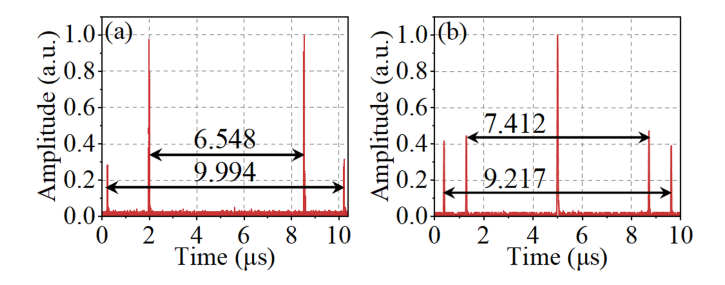


Fig. 8. The experimentally observed temporal waveforms of the generated electrical pulses for (a) 13.6 GHz and (b) 27.7 GHz.

respectively. The output electrical pulse waveforms are shown in Fig. 10(b), (c), and (d), respectively. The experimentally measured frequencies of 10.009 and 14.994 GHz, 10.009 and 26.002 GHz, and 10.001 and 27.989 GHz are obtained accordingly. Thus, the ability of multiple frequency identification is experimentally proved.

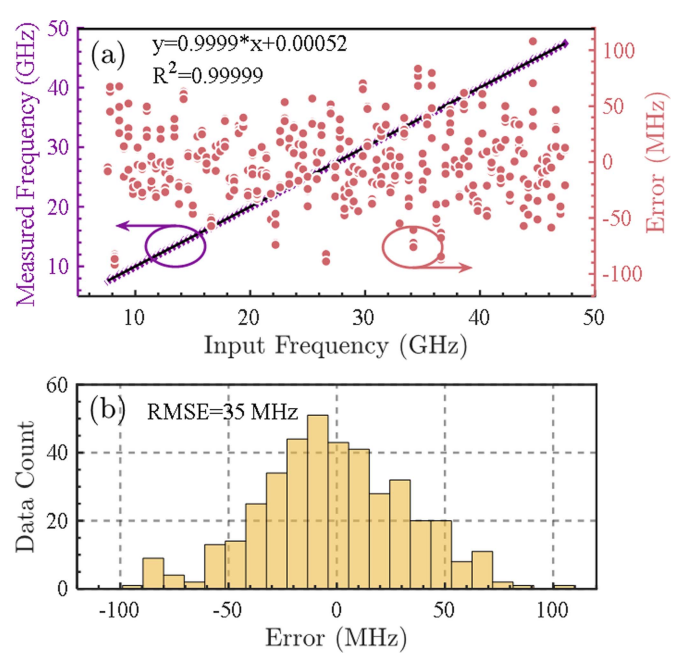


Fig. 9. (a) The experimentally measured frequency results versus the input frequency; (b) the experimentally obtained measurement error histogram. The SUTs are single-frequency signals.

# D. Frequency Measurement Resolution

The frequency measurement resolution is dependent on the chirp rate of the optical sideband and the 6-dB bandwidth of the EBPF. The sweeping period of the -1st-order optical sideband is  $10~\mu s$ . The frequency response of the used EBPF is measured and shown in Fig. 11, for which the center frequency is 3 GHz, and the 6-dB bandwidth is 31 MHz.

Fig. 12(a) shows the experimentally obtained pulse waveforms when the actual input microwave signals have frequencies of 12.20 and 12.29 GHz. The sampling rate of the oscilloscope is 2.5 GSa/s, which is the same as that used for verifying the measurement accuracy. Two pairs of electrical pulses with time intervals of 7.5136 and 7.4288  $\mu$ s are distinguished, respectively. According to Fig. 6, the measured frequencies 12.217 and 12.326 GHz are obtained, respectively. As shown in the inset of Fig. 12(a), the measured FWHM of the pulse is 30.3 ns. The two adjacent pulses are separated by 38 ns and can be identified clearly. Therefore, the frequency resolution of 90 MHz is experimentally achieved.

The frequency resolution can be optimized by increasing the sweeping period of the -1st-order optical sideband. In the experiments, this period is changed to 50  $\mu$ s. Note that if the measured frequencies are estimated from the mapping curves in Fig. 6, the time interval corresponding to T of 50  $\mu$ s needs to be divided by 5 in advance. Two microwave signals with frequencies of 12.70 and 12.74 GHz are injected into MZM2. The output pulse waveform is shown in Fig. 12(b). Two pairs of pulses can be clearly distinguished, with time intervals of 35.805 and 35.64  $\mu$ s, respectively. The measured frequencies are 12.718 and 12.765 GHz, respectively. Therefore, the improved frequency resolution of 40 MHz is achieved.

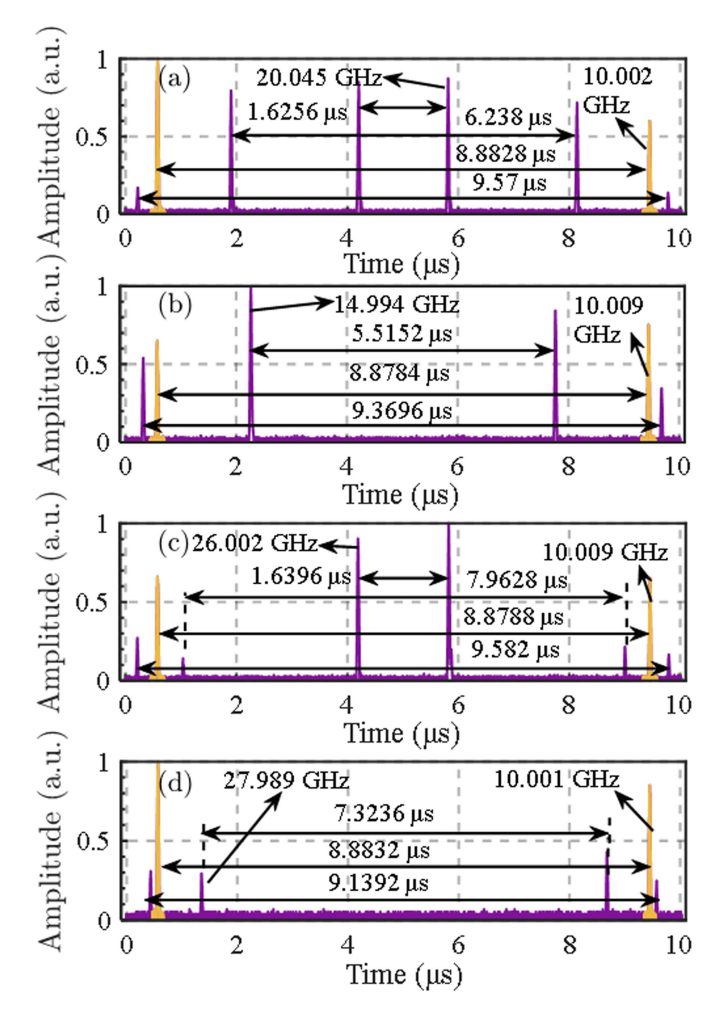


Fig. 10. The output electrical pulse waveforms when the frequencies of the input two-tone RF signal are (a) 10 and 20 GHz, (b) 10 and 15 GHz, (c) 10 and 26 GHz, and (d) 10 and 28 GHz.

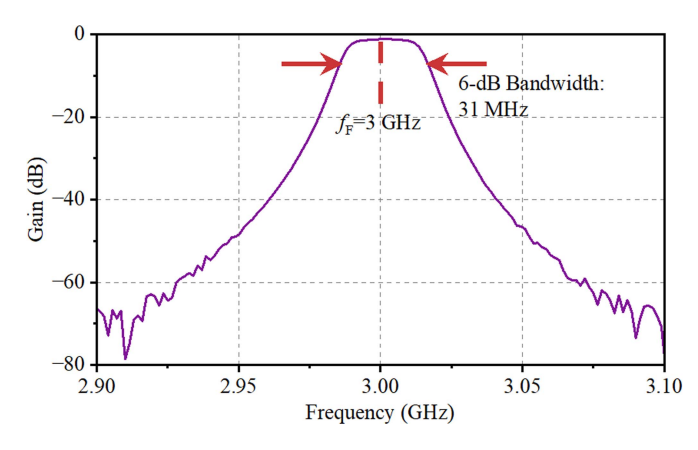


Fig. 11. The experimentally measured frequency response of the used EBPF.

In the experiment, the frequency sweeping is nonlinear, and the chirp rate of the 2nd-order frequency-sweeping optical sideband is twice that of the 1st-order sideband. Thus, the system exhibits different frequency resolutions for distinct input frequencies. Fig. 13 illustrates the frequency measurement resolutions of different frequencies under test corresponding to each

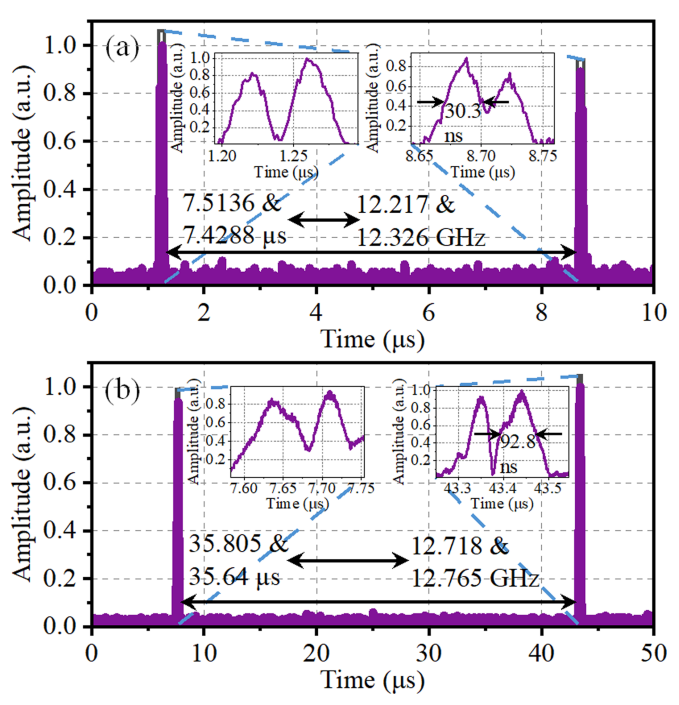


Fig. 12. The experimentally obtained output electrical pulse waveforms when the actual input frequencies are (a) 12.20 and 12.29 GHz, and (b) 12.70 and 12.74 GHz.

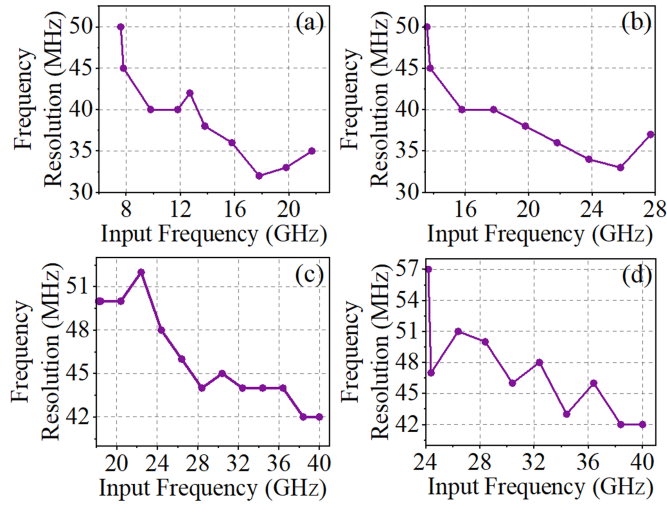


Fig. 13. The pulse widths and frequency measurement resolutions of different frequencies under test corresponding to (a) FTTM1, (b) FTTM2, (c) FTTM3, and (d) FTTM4, with the sweeping period of  $50 \mu s$ .

FTTM when the sweeping period of the optical sideband is 50  $\mu$ s. In Fig. 13(a), the frequency resolution varies from 32 to 50 MHz for the frequency range of 7.6 to 21.7 GHz, corresponding to the whole FTTM1 curve in Fig. 6. While in Fig. 13(b), the frequency resolution varies from 33 to 50 MHz for the frequency range of 13.6 to 27.7 GHz, corresponding to the whole FTTM2 curve in Fig. 6.

For the frequency range of 18.2 to 40 GHz as shown in Fig. 13(c), the frequency resolution varies from 42 to 52 MHz, corresponding to the whole FTTM3 curve in Fig. 6. And for the frequency range of 24.2 to 40 GHz corresponding to the whole

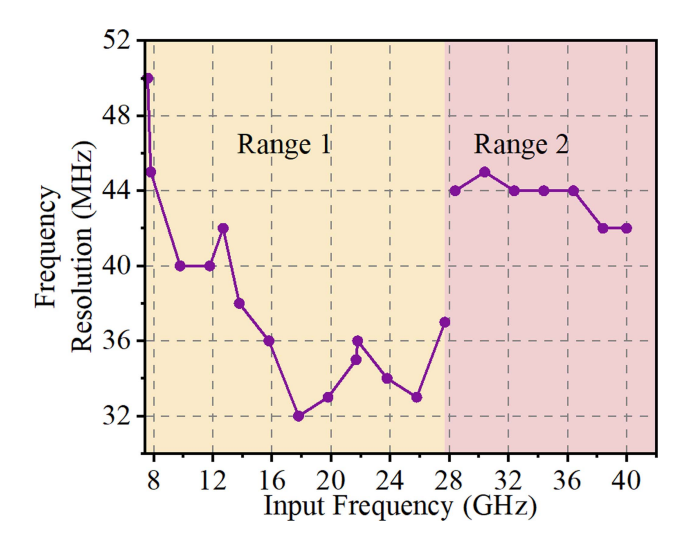


Fig. 14. The experimentally obtained optimized frequency resolution performance for the frequency range from 7.6 to 40 GHz for the sweeping period of 50  $\mu$ s.

FTTM4 curve in Fig. 6, the frequency resolution varies from 42 to 57 MHz, as shown in Fig. 13(d). It should be mentioned that the frequency resolution performance from 40 to 47.4 GHz is not experimentally measured here, due to the lack of two microwave sources in this frequency range.

The frequency resolution is improved with the decreasing of the used optical sideband chirp rate. FTTM3 and FTTM4 correspond to the 2nd-order optical sidebands, while FTTM1 and FTTM2 correspond to the 1st-order optical sidebands, having smaller chirp rates. Thus, the frequency resolution performances in Fig. 13(a) and (b) are better than those in Fig. 13(c) and (d) The variation of the frequency resolution corresponding to each FTTM curve is mainly due to the nonlinearity of the frequency sweeping optical sidebands. As shown in Fig. 5, although the driving signal has been optimized to improve the linearity of the frequency sweeping optical sideband, the nonlinearity still exists.

In ranges (b) to (f) shown in Fig. 6, each input frequency will correspond to parts of different FTTM curves. The frequency resolution is determined by the optimized one. Taking the input frequency of 20 GHz located at range (c) as an example, as shown in Fig. 13(a)–(c), the frequency resolution of 36, 38, and 50 MHz is respectively achieved in the parts of FTTM1, FTTM2, and FTTM3. The actual frequency resolution of 20 GHz should be 36 MHz, which is the optimal value in all FTTMs.

By this means, the actual frequency resolution performance for the frequency range from 7.6 to 40 GHz is obtained as shown in Fig. 14. As can be seen, the entire resolution curve can be divided into two parts with the frequency of 27.7 GHz as the boundary. This frequency is the maximum frequency that can be measured by the 1st-order optical sideband, which is also the maximum frequency for FTTM2. Since the chirp rates of the optical sideband for FTTM3 and FTTM4 are twice that of FTTM1 and FTTM2, the frequency resolution performance for the frequencies lower than 27.7 GHz is better than that for the frequencies higher than 27.7 GHz. In each range, the resolution

TABLE I

COMPARISON OF PHOTONICS-BASED MICROWAVE FREQUENCY MEASUREMENT
METHODS

			R (CU <sub>2</sub> )	Number of	Number	Used
	$\delta f(\text{MHz})^{-1}$	$T_{\rm s}$ (µs) $^2$	$D_{\rm m}$ (GHz)	FTTM	of	Devices
				curves	channels	Number
[13]	700	0.1	40	1	1	8
[14]	70	0.01	30	1	1	7
[16]	200	22.8	20	1	1	19
[17]	70	10	10	1	1	9
[18]	40	5e4	10	1	1	10
[19]	70	160	12	1	1	10
[20]	60	4	4	1	1	17
[22]	35	4	10	5	1	29
[23]	/	10	28	2	2	17
This Work	32~50	50	39.8	4	1	19

<sup>&</sup>lt;sup>1</sup> Frequency resolution.

decreases as the frequency increases. This is because the rate of frequency sweeping decreases with the increasing of frequency, as shown in Fig. 5(c). The overall frequency resolution varies between 32 and 50 MHz. By employing linearly frequency-sweeping optical signals, the constant frequency resolution can be achieved.

As can be seen, the frequency resolution varies between 32 and 50 MHz for the sweeping period of 50  $\mu$ s, while the maximum error shown in Fig. 9 is 108 MHz for the sweeping period of 10  $\mu$ s. This is because the measurement error is mainly due to frequency drift of the lasers, which may cause two adjacent pulses shift together while keeping identified.

Table I shows a comparison of this work with the reported photonics-based microwave frequency measurement methods, where the system complexity is defined as the number of devices in the system. The method proposed in this work has experimentally achieved 4 FTTM curves in a single channel with 19 devices. The frequency measurement range is 7.6 to 47.4 GHz, and the frequency resolution is better than 50 MHz. The proposed system has advantages in terms of frequency resolution, measurement bandwidth, and system complexity.

### E. Discussions

For the multiple frequency measurement condition, the measurement ambiguity can be resolved by introducing another FTTM relationship. One way is to introduce a frequency shift to the optical carrier. For instance, an initial frequency shift can be introduced to the optical carrier before it is modulated by the SUTs at MZM2. The initial frequency shift introduced to the optical carrier ultimately results in the common shift of the four FTTM curves on the frequency axis. The two mapping relationships before and after the frequency shift have different measurement ambiguities. By comparing the measurement results of the two conditions with and without frequency shift, the correct frequency information can be identified to solve the ambiguity problem for multiple frequencies measurement.

<sup>&</sup>lt;sup>2</sup> Time resolution.

<sup>&</sup>lt;sup>3</sup> Measurement bandwidth.

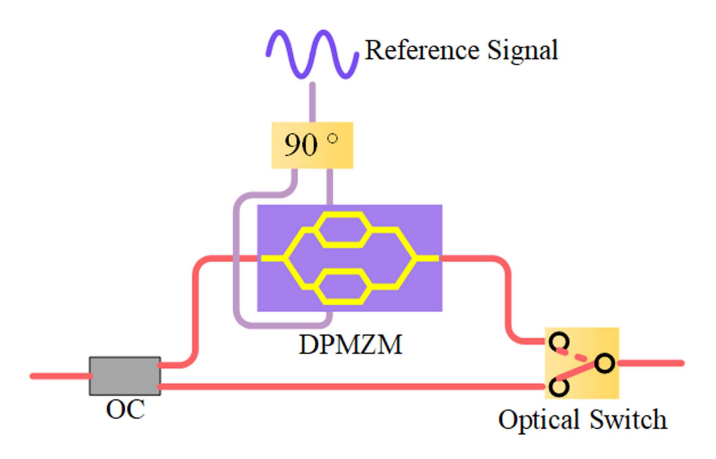


Fig. 15. Schematic of carrier control architecture in the lower branch for resolving measurement ambiguity. DPMZM: dual-parallel Mach–Zehnder modulator.

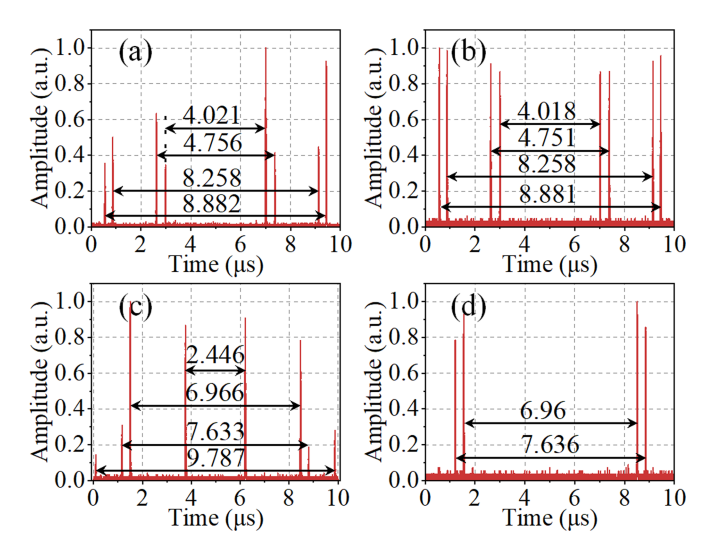


Fig. 16. The output electrical pulse waveforms when the frequencies of the input multi-tone RF signal are (a) 16.016, 17.006, and 23 GHz, (b) 16.016 and 17.006 GHz; (c) and (d): The versions of (a) and (b) after the frequency shift is introduced to the optical carrier.

Experiments are taken. As shown in Fig. 15, the frequency shift is achieved by using a dual-parallel Mach–Zehnder modulator (DPMZM) biased at the carrier-suppressed single sideband modulation point [22]. An optical switch can be utilized to select the optical carriers before and after the frequency shift to be injected into MZM2. The optical switch selects the frequency-shifted optical carrier to enter MZM2 at the beginning of the next sweeping period. By comparing the measurement results of the two periods with and without frequency shift, the correct frequency information can be identified.

When taking a positive frequency shift with the optical carrier of 4 GHz, the four FTTM curves shown in Fig. 6 collectively shift 4 GHz in the positive direction on the frequency axis. The frequency measurement range is changed to  $11.6\sim51.4$  GHz. The unambiguous measurement range is the intersection of the measurement ranges with and without the frequency shift, which is  $11.6\sim47.4$  GHz.

Without frequency shift, Fig. 16(a) shows the generated pulses when the input SUT (SUT1) has the frequencies of 16.016, 17.006, and 23 GHz. In Fig. 16(b), the input SUT (SUT2) has the frequencies of 16.016 and 17.006 GHz. It can be seen that the pulse distributions illustrated in Fig. 16(a) and (b) are identical. This is because the pulses generated by 17.006 GHz and 16.016 GHz can be combined to form the pulse distribution corresponding to 23 GHz. For the results in Fig. 16(a) and (b), all possible frequencies are  $\mathbf{f_a} = [15.981, 17.004, 22.944, 43.012]$  and  $\mathbf{f_b} = [15.985, 17.006, 22.948, 43.020]$  (GHz), respectively.

By taking the frequency shift of 4 GHz to the optical carrier, the pulse waveforms generated by the corresponding three frequencies and two frequencies are shown in Fig. 16(c) and (d), respectively. The obtained pulse waveforms are no longer identical. By adding the initial frequency shift of 4 GHz to the FTTM curves shown in Fig. 6, for the results in Fig. 16(c) and (d), all possible frequencies are  $\mathbf{f_c} = [22.943, 16.019, 16.998, 51.102]$  and  $\mathbf{f_d} = [16.015, 17.006]$  (GHz), respectively.

Thus, the actual frequencies of SUT1 should be the intersection of the measurement results corresponding to Fig. 16(a) and (c), which is [22.944, 16.000, 17.001] (GHz). Here the final measurement results are the average values of the similar elements in  $f_{\rm a}$  and  $f_{\rm c}.$  In the same way, the actual frequencies of SUT2 are [16.000, 17.006] (GHz) by averaging the similar elements in  $f_{\rm b}$  and  $f_{\rm d}.$  In this way, the measurement ambiguity for multiple frequencies can be resolved.

The processing latency contains the system link transmission latency of the SUT, the sweeping period, and the latency of the digital signal processing. The system link transmission latency of the SUT is measured to be 326 ns by using the method proposed in [28]. The latency of the digital signal processing is about several ms. Although a single-frequency SUT involves analyzing numerous pulses, the number of sampling points of each sweeping period is 25000 with a sampling rate of 2.5 GSa/s in the experiments, which is not large. Besides, complex digital signal processing is not required. Therefore, the processing latency doesn't increase significantly with the increase in the number of pulses. The processing latency can be optimized by reducing the lengths of the used optical fibers and RF cables, using digital signal processor with high speed. The system can also be integrated to further optimize the latency.

By using the bidirectional frequency-sweeping optical sidebands, pairs of pulses will be generated. Through analyzing the time interval between each pair of pulses, the frequency can be obtained. If only analyzing the pulses generated by the unidirectional frequency-sweeping optical sideband, the absolute time for each pulse should be analyzed. The complexities of the two methods have not too much difference. Besides, if unidirectional frequency sweeping with half the time period of the bidirectional one is leveraged, the amount of data will be halved, resulting in reduced processing latency. However, the very accurate time synchronization between the frequencysweeping source and the analog-to-digital converter, or an additional reference signal, needs to be introduced.

If using higher-order frequency-sweeping optical sidebands, a larger measurement bandwidth can be achieved, resulting in higher computational complexity. The working bandwidth and the complexity should be taken into comprehensive consideration in actual applications. The system can be integrated to reduce the size, weight, and power. For the system integration, the integration of the optical circulator is challenging, which can be implemented based on silicon microrings [30].

### IV. CONCLUSION

In conclusion, a microwave photonic frequency measurement scheme with a large working bandwidth enabled by multiple FTTM curves is proposed and demonstrated. The microwave signal to be measured is mixed with multiple frequencysweeping signals simultaneously with the help of photonic techniques. Multiple FTTM curves are introduced in a single channel. By jointly exploiting the multiple FTTM curves, the frequency to be measured is mapped to the number and time positions of the low-speed electrical pulses. The measurement bandwidth is effectively increased without reducing the time resolution or frequency resolution. In the experiment, four FTTM curves are achieved by using the -1st and the -2nd-order optical sidebands generated from a semiconductor laser working in the period-one state. A frequency measurement range of 7.6 to 47.4 GHz is realized with a measurement bandwidth of 39.8 GHz. The frequency resolution is better than 50 MHz when the sweeping period is 50  $\mu$ s. The proposed scheme can provide key techniques for wideband electronic spectrum monitoring applications.

#### REFERENCES

- [1] D. Zhu and S. Pan, "Broadband cognitive radio enabled by photonics," *J. Lightw. Technol.*, vol. 38, no. 12, pp. 3076–3088, Jun. 2020.
- [2] D. Zhu et al., "Microwave photonic cognitive radar with a subcentimeter resolution," *IEEE Trans. Microw. Theory Techn.*, vol. 72, no. 9, pp. 5519–5529, Sep. 2024.
- [3] S. Pan and J. Yao, "Photonics-based broadband microwave measurement," J. Lightw. Technol., vol. 35, no. 16, pp. 3498–3513, Aug. 2017.
- [4] A. E. Spezio, "Electronic warfare systems," *IEEE Trans. Microw. Theory Techn.*, vol. 50, no. 3, pp. 633–644, Mar. 2002.
- [5] L. Wang, X. Wang, and S. Pan, "Microwave photonics empowered integrated sensing and communication for 6G," *IEEE Trans. Microw. Theory Techn.*, vol. 73, no. 8, pp. 5295–5315, Feb. 2025, doi: 10.1109/TMTT.2025.3532810.
- [6] X. Zou, B. Lu, W. Pan, L. Yan, A. Stöhr, and J. Yao, "Photonics for microwave measurements," *Laser Photon. Rev.*, vol. 10, no. 5, pp. 711–734, Jul. 2016.
- [7] X. Zou, S. Pan, and J. Yao, "Instantaneous microwave frequency measurement with improved measurement range and resolution based on simultaneous phase modulation and intensity modulation," *J. Lightw. Technol.*, vol. 27, no. 23, pp. 5314–5320, Dec. 2009.
- [8] Z. Rabbani, M. Ganjali, and S. E. Hosseini, "Microwave photonic IFM receiver with adjustable measurement range based on a dual-output Sagnac loop," J. Lightw. Technol., vol. 42, no. 1, pp. 106–112, Jan. 2024.
- [9] B. Zhu, W. Zhang, S. Pan, and J. Yao, "High-sensitivity instantaneous microwave frequency measurement based on a silicon photonic integrated fano resonator," *J. Lightw. Technol.*, vol. 37, no. 11, pp. 2527–2533, Jun. 2019.
- [10] Y. Tao et al., "Fully on-chip microwave photonic instantaneous frequency measurement system," *Laser Photon. Rev.*, vol. 16, no. 11, Aug. 2022, Art. no. 2200158.
- [11] L. Liu and Z. Yu, "Low error and broadband microwave frequency measurement using a silicon Mach–Zehnder interferometer coupled ring array," J. Lightw. Technol., vol. 41, no. 19, pp. 6126–6133, Oct. 2023.

- [12] X. Xie et al., "Broadband photonic radio-frequency channelization based on a 39-GHz optical frequency comb," *IEEE Photon. Technol. Lett.*, vol. 24, no. 8, pp. 661–663, Apr. 2012.
- [13] B. Zhang et al., "Impact of dispersion effects on temporal-convolution-based real-time fourier transformation systems," *J. Lightw. Technol.*, vol. 38, no. 17, pp. 4664–4676, Sep. 2020.
- [14] J. Ding, D. Zhu, Z. Wang, B. Zhang, T. Lu, and S. Pan, "Photonic real-time Fourier transform based on frequency stretching of RF signals," in *Proc. 2021 IEEE Int. Topical Meeting Microw. Photon.*, Pisa, Italy, 2021, pp. 1–3.
- [15] T. Lu, D. Zhu, J. Ding, B. Ni, X. Liu, and S. Pan, "Photonic time compressing assisted real-time Fourier transform system," in *Proc. 2023 Asia Commun. Photon. Conf./2023 Int. Photon. Optoelectronics Meetings*, Wuhan, China, 2023, pp. 1–3.
- [16] B. Zhu, J. Tang, W. Zhang, S. Pan, and J. Yao, "Broadband instantaneous multi-frequency measurement based on a Fourier domain mode-locked laser," *IEEE Trans. Microw. Theory Techn.*, vol. 69, no. 10, pp. 4576–4583, Oct. 2021.
- [17] L. Wang et al., "Compact multi-tone microwave photonic frequency measurement based on a single modulator and frequency-to-time mapping," *J. Lightw. Technol.*, vol. 40, no. 19, pp. 6517–6522, Oct. 2022.
- [18] G. Wang et al., "Photonic-assisted multiple microwave frequency measurement with improved robustness," *Opt. Lett.*, vol. 48, no. 5, pp. 1172–1175, Mar. 2023.
- [19] X. Chen et al., "Precise multiple frequency identification based on frequency-to-time mapping and cross-correlation," *J. Lightw. Technol.*, vol. 41, no. 18, pp. 5895–5901, Sep. 2023.
- [20] P. Zuo, D. Ma, and Y. Chen, "Short-time Fourier transform based on stimulated Brillouin scattering," *J. Lightw. Technol.*, vol. 40, no. 15, pp. 5052–5061, Aug. 2022.
- [21] Y. Yao et al., "Highly integrated dual-modality microwave frequency identification system," *Laser Photon. Rev.*, vol. 16, no. 10, Oct. 2022, Art. no. 2200006.
- [22] X. Li, T. Shi, D. Ma, and Y. Chen, "Channelized analog microwave short-time Fourier transform in the optical domain," *IEEE Trans. Microw. Theory Techn.*, vol. 72, no. 5, pp. 3210–3220, May 2024.
- [23] J. Shi, F. Zhang, Y. Zhou, S. Pan, Y. Wang, and D. Ben, "Photonic scanning receiver for wide-range microwave frequency measurement by photonic frequency octupling and in-phase and quadrature mixing," *Opt. Lett.*, vol. 45, no. 19, pp. 5381–5384, Sep. 2020.
- [24] S. -K. Hwang, J. -M. Liu, and J. K. White, "Characteristics of period-one oscillations in semiconductor lasers subject to optical injection," *IEEE J. Sel. Topics Quantum Electron.*, vol. 10, no. 5, pp. 974–981, Sep./Oct. 2004.
- [25] P. Zhou, F. Zhang, and S. Pan, "Generation of linear frequency-modulated waveforms by a frequency-sweeping optoelectronic oscillator," *J. Lightw. Technol.*, vol. 36, no. 18, pp. 3927–3934, Sep. 2018.
- [26] S. Zhang, P. Zuo, and Y. Chen, "Microwave photonic time-frequency analysis based on period-one oscillation and phase-shifted fiber Bragg grating," *IEEE Microw. Wireless Technol. Lett.*, vol. 34, no. 1, pp. 135–138, Jan. 2024.
- [27] J. Yu et al., "Tunable multi-band linear frequency modulated waveforms generation based on self-subharmonic modulating of optically injected semiconductor laser," *IEEE Photon. J.*, vol. 17, no. 2, Apr. 2025, Art. no. 5500307.
- [28] J. Yu et al., "Multiple frequency measurement based on self-oscillating and subharmonic modulating of optically injected semiconductor laser," Opt. Laser Technol., vol. 186, Aug. 2025, Art. no. 112625.
- [29] Z. Lei, "The investigation of the measurement technology based on optical dispersion," M.S. thesis, Dept. Electron. Commun. Eng., Nanjing Univ. Aeronaut. Astronaut., Nanjing, China, 2021.
- [30] D. Huang et al., "Dynamically reconfigurable integrated optical circulators," *Optica*, vol. 4, no. 1, pp. 23–30, Jan. 2017.

**Boyang Ni** received the B.S. degree in information engineering in 2022, from the Nanjing University of Aeronautics and Astronautics, Nanjing, China, where he is currently working toward the Ph.D. degree.

His research focuses on microwave photonic processing.

Dan Zhu received the B.S. and Ph.D. degrees in electronic engineering from Tsinghua University, Beijing, China, in 2004 and 2009, respectively. In 2011, she joined the College of Electronic and Information Engineering, Nanjing University of Aeronautics and Astronautics, Nanjing, China, where she is currently a Professor. From 2014 to 2015, she was a Visiting Scholar with Microwave Photonics Research Laboratory, University of Ottawa, Ottawa, ON, Canada. Her current research interests include microwave photonic signal processing and system applications.

**Zhouyang Pan** received the B.S. degree in electronic science and technology from the Nanjing University of Aeronautics and Astronautics, Nanjing, China, in 2021, where he is currently working toward the Ph.D. degree.

His research focuses on microwave photonic processing.

**Jiewen Ding** received the B.S. degree in electronic science and technology in 2019, from the Nanjing University of Aeronautics and Astronautics, Nanjing, China, where he is currently working toward the Ph.D. degree.

His research focuses on microwave photonic processing.

Shilong Pan (Fellow, IEEE) received the B.S. and Ph.D. degrees in electronic engineering from Tsinghua University, Beijing, China, in 2004 and 2008, respectively. From 2008 to 2010, he was a "Vision 2010" Postdoctoral Research Fellow with the Microwave Photonics Research Laboratory, University of Ottawa, Ottawa, ON, Canada. In 2010, he joined the Nanjing University of Aeronautics and Astronautics, Nanjing, China, where he is currently a Full Professor and the Director of National Key Laboratory of Microwave Photonics.

He has authored or coauthored more than 350 papers in peer-reviewed journals and 300 papers in conference proceedings. His research focuses on microwave photonics.

Prof. Pan is currently a Senior Editor of *PhotoniX*, an Associate Editor for IEEE/Optica JOURNAL OF LIGHTWAVE TECHNOLOGY and IEEE TRANSACTIONS ON MICROWAVE THEORY AND TECHNIQUES, and is currently the Vice Chair of IEEE MTT-22 Microwave Photonics. He was also the Chair of a number of international conferences, symposia, and workshops, including the TPC Chair of the International Conference on Optical Communications and Networks in 2015, the TPC chair of IEEE International Topical Meeting on Microwave Photonics (MWP) in 2023, a TPC Co-chair of IEEE MWP 2017, and the General Co-Chair of IEEE MWP 2021 and 2025.

He is a Fellow of Optica, SPIE and IET. He was selected as an IEEE Photonics Society Distinguished Lecturer in 2019 and an IEEE MTT-S Distinguished Microwave Lecturer in 2022. He was the recipient of IEEE MTT-S Outstanding Young Engineer Award in 2021.